2014-06-04

Numerical Modal Analysis of Composite Structures Coupled With Water

Kwon, Y. W.

Elsevier Ltd.

Composite Structures 116 (2014), 325-335
http://hdl.handle.net/10945/48287

Composite Structures 116 (2014) 325–335

Contents lists available at ScienceDirect

Composite Structures

journal homepage: www.elsevier.com/locate/compstruct

Numerical modal analysis of composite structures coupled with water

Y.W. Kwon *, S.D. Plessas

Dept. of Mechanical & Aerospace Engineering, Naval Postgraduate School, Monterey, CA 93943, United States

ARTICLE INFO

Article history:
Available online 4 June 2014

Keywords:
Fluid–Structure Interaction
Modal analysis
Multiphysics analysis

ABSTRACT

Dynamic characteristics of polymer composite beam and plate structures were studied when the structures were coupled with water. The effect of Fluid–Structure Interaction (FSI) on natural frequencies, mode shapes, and dynamic responses was examined for polymer composite structures using multiphysics-based computational techniques. Composite structures were modeled using the Finite Element Method. The fluid was modeled as an acoustic medium using the Cellular Automata and finite element techniques. Those techniques were coupled so that both fluid and structure could interact bi-directionally. In order to make the coupling easier, the beam and plate finite elements have only displacement degrees of freedom but no rotational degrees of freedom. Then, the numerical modal analysis technique was applied to the composite structures with and without FSI, respectively, so that the effect of FSI can be examined by comparing the two results. The study showed that the effect of FSI is significant on dynamic properties of polymer composite structures. Some previous experimental observations were confirmed using the numerical modal analysis.

Published by Elsevier Ltd.

1. Introduction

Composite materials have been of great interest recently as they prove to have many significant advantages over the 'traditional' materials in shipbuilding, marine, and aerospace industry applications. They possess many beneficial properties, which include, but are not limited to, their superior specific strength and specific stiffness, their excellent resistance to corrosion and marine environmental deterioration, and their ability to conform any shape that designers wish to make. As a result, composite structures have been used in many military and civilian applications. Additionally, a rise in interest in composites is expected to occur in the near future for use in building fuel-efficient and therefore cost-efficient naval ships, vessels, and marine structures.

The vast majority of the past research on composite structures has been conducted for dry structures. A limited amount of research has been undertaken with considerations of the interaction between composite structures and fluids such as water. Some of the Fluid–Structure Interaction (FSI) studies with composite structures were liquid sloshing in composite tanks [1,2]. Other FSI studies were composite structures subjected to underwater explosion [3,4]. More recently, a series of studies have been conducted to understand the effect of FSI on composite structures [5–10]. In those research, responses of composite structures were compared between the two cases with (i.e., in water) and without (i.e., in air) the FSI effect under impact or cyclic loading. The results showed that the effects of FSI on polymer composite structures are significant because densities of polymer composites are very comparable to that of water. The effect of FSI can lead to a premature failure of a composite structure if the effect is not considered in the design and analysis of composite structures.

The previous studies on the FSI effect revealed some results to be noteworthy. When a polymer composite structure was loaded in air and water, respectively, under the same dynamic loading condition, the FSI effect with water resulted in a larger stress in the composite structure. Additionally, the location of the maximum stress could be shifted because of the FSI effect. For example, when a clamped polymer composite plate was impacted in air and water, respectively, the strain gage reading at different locations of the plate showed a drastic difference between the two different impact cases. In other words, the strain responses near the center of the composite plate were qualitatively similar even though there were some differences in magnitudes and phases because of the FSI effect. On the other hand, the strain–time history readings at the location near the clamped corner were significantly different qualitatively and quantitatively between the two impact cases. Fig. 1 compares the strain responses at the two locations. The results suggest that the effect of the added mass is not uniform over the composite plate.

In order to further understand the effect of the added mass resulting from FSI, an experimental study was conducted for polymer composite beams [9]. Free vibrational motions of an e-glass composite beam were measured in air and water, respectively,

* Corresponding author. Tel./fax: +1 831 656 3468x2238.
E-mail address: ywkwon@nps.edu (Y.W. Kwon).

http://dx.doi.org/10.1016/j.compstruct.2014.05.032
0263-8223/Published by Elsevier Ltd.

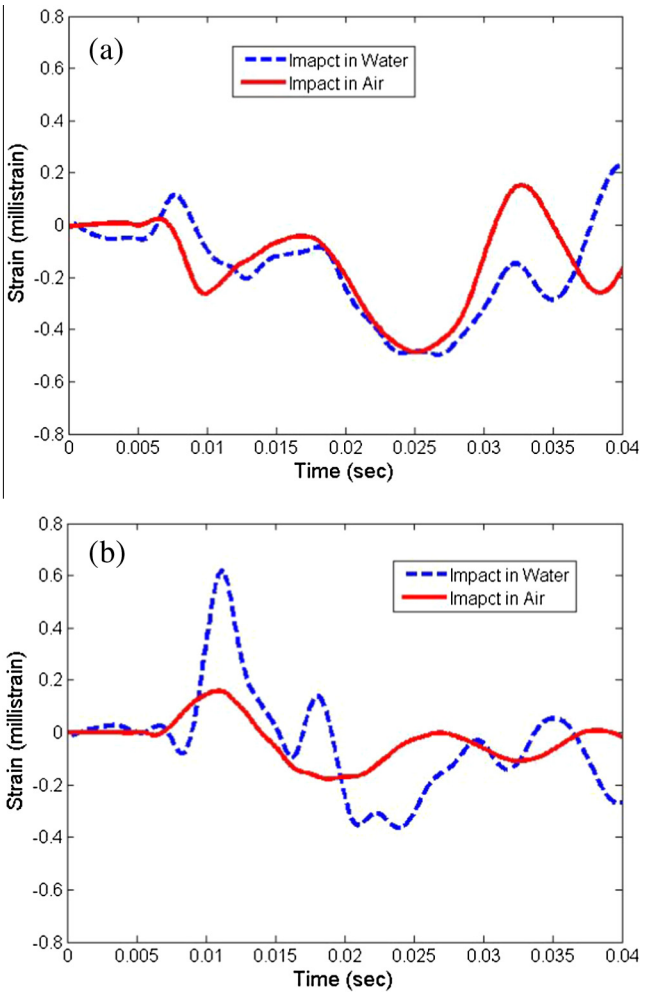

Fig. 1. Comparison of strain–time history plots of a clamped composite plate subjected to central impact loading while the plate is in air and water, respectively. (a) Strains near the center of the plate and (b) strains near the corner of the plate.

using the Digital Image Correlation (DIC) technique. Additionally, modal parameters like natural frequencies, mode shapes and modal curvatures were obtained when a carbon composite beam was in air and water, respectively.

The present study is similar to that in Ref. [9]. A series of numerical experimental studies were conducted for composite beams and plates. In order to measure mode shapes of composite structures accurately, many sensors must be attached to the structure for a physical experiment. However, numerical experiments can be conducted easily with a reasonable mesh of the structure. Therefore, numerical modal analyses were conducted in this study to enhance the understanding of the effect of the added mass on dynamic behaviors of polymer composite beams and plates.

The next section describes computational techniques used for the study. Both the Finite Element Method (FEM) and Cellular Automata (CA) technique were used. The following section shows some examples to verify the program. Then, the study of added mass effect is presented for composite plates and beams, which was subsequently followed by conclusions.

2. Computational modeling

2.1. Multiphysics analysis

A multiphysics-based computational analysis is conducted for this study. Beams and plates were modeled using the Finite Element Method (FEM). In order to make the coupling between the structure and fluid easy, the beam and plate elements have only displacement degrees of freedom like 3-D solid finite elements. As a result, those elements represent the thickness dimension explicitly so that fluid at the bottom and top surfaces can be readily separated by the structure. Additionally, the compatibility conditions at the fluid–structure interfaces can be applied easily. The fluid is considered as an acoustic domain by neglecting fluid flow, viscosity, etc. The governing equation for a linear acoustic field is solved using both FEM and the Cellular Automata (CA) techniques. After time domain solutions are obtained from the multiphysics analysis, the Fast Fourier Transform (FFT) is applied so as to transform the time domain to the frequency domain as the numerical modal analysis. Then, modal parameters of the dynamic structure are determined. The details of the analysis techniques used in this study are discussed below.

2.2. Structural finite element analysis

Since beam and plate finite elements can be easily derived from shell finite elements, this section describes the general shell element formulation. The detailed formulation of the solid-like shell finite element was given in Ref. [11] and it is briefly presented here. The plate/shell element is sketched in Fig. 2 which has eight nodes like a 3-D brick element. There are two nodes along the thickness of the shell because linear interpolations of displacements are mostly good enough along the thickness. However, more nodes can be added to the inplane dimension to improve the accuracy. Such high order shell elements can be developed from the present element in a straightforward matter so that the eight-node element is discussed here. Since the element has nodal displacements at both top and bottom surfaces, the elements can be stacked together to represent a laminated composite. Additionally, fluid on either side of the shell can be readily separated, and the compatibility conditions can be applied at the fluid–structure interface easily because both media can have nodes at the same spatial position.

The mathematical formulation of the shell element is based on a high-order bending theory which includes bending strains, transverse shear strains, and the transverse normal strain. The element stiffness matrix in terms of its local axes is expressed as

$$[K_{local}] = \int_{\Omega^e} [B_b]^T [D_b][B_d] d\Omega + \int_{\Omega^e} [B_s]^T [D_s][B_s] d\Omega + \int_{\Omega^e} [B_z]^T D_z [B_z] d\Omega \quad (1)$$

where the matrix related to the bending strains is expressed as

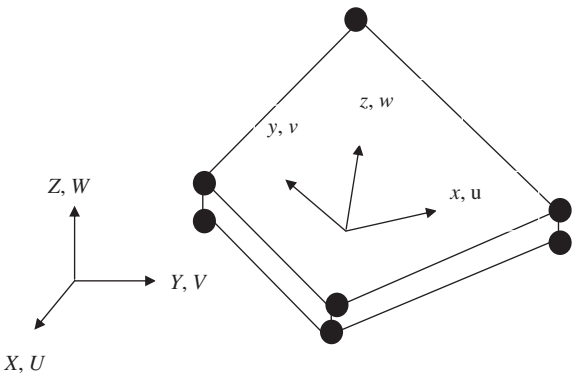

Fig. 2. Eight-node shell element. The lower cases indicate the local coordinate system while the upper cases denote the global coordinate system.

$$[B_b] = [\,B_{b1} \quad B_{b2}\,] \tag{2}$$

$$[B_{bi}] = \begin{bmatrix} H_i\frac{\partial N_1}{\partial x} & 0 & 0 & H_i\frac{\partial N_2}{\partial x} & 0 & 0 & H_i\frac{\partial N_3}{\partial x} & 0 & 0 & H_i\frac{\partial N_4}{\partial x} & 0 & 0 \\ 0 & H_i\frac{\partial N_1}{\partial y} & 0 & 0 & H_i\frac{\partial N_2}{\partial y} & 0 & 0 & H_i\frac{\partial N_3}{\partial y} & 0 & 0 & H_i\frac{\partial N_4}{\partial y} & 0 \\ H_i\frac{\partial N_1}{\partial y} & H_i\frac{\partial N_1}{\partial x} & 0 & H_i\frac{\partial N_2}{\partial y} & H_i\frac{\partial N_2}{\partial x} & 0 & H_i\frac{\partial N_3}{\partial y} & H_i\frac{\partial N_3}{\partial x} & 0 & H_i\frac{\partial N_4}{\partial y} & H_i\frac{\partial N_4}{\partial x} & 0 \end{bmatrix} \tag{3}$$

and the matrix associated with the transverse shear strains is shown as

$$[B_s] = [\,B_{s1} \quad B_{s2}\,] \tag{4}$$

$$[B_{si}] = \begin{bmatrix} N_1\frac{\partial H_i}{\partial z} & 0 & H_i\frac{\partial N_1}{\partial x} & N_2\frac{\partial H_i}{\partial z} & 0 & H_i\frac{\partial N_2}{\partial x} & N_3\frac{\partial H_i}{\partial z} & 0 & H_i\frac{\partial N_3}{\partial x} & N_4\frac{\partial H_i}{\partial x} & 0 & H_i\frac{\partial N_4}{\partial x} \\ 0 & N_1\frac{\partial H_i}{\partial z} & H_i\frac{\partial N_1}{\partial y} & 0 & N_2\frac{\partial H_i}{\partial z} & H_i\frac{\partial N_2}{\partial y} & 0 & N_3\frac{\partial H_i}{\partial z} & H_i\frac{\partial N_3}{\partial y} & 0 & N_4\frac{\partial H_i}{\partial z} & H_i\frac{\partial N_4}{\partial y} \end{bmatrix} \tag{5}$$

$$[B_z] = [\,B_{z1} \quad B_{z2}\,] \tag{6}$$

In addition, the matrix for the transverse normal strain is

$$[B_{zi}] = \left[\,0 \quad 0 \quad N_1\frac{\partial H_i}{\partial z} \quad 0 \quad 0 \quad N_2\frac{\partial H_i}{\partial z} \quad 0 \quad 0 \quad N_3\frac{\partial H_i}{\partial z} \quad 0 \quad 0 \quad N_4\frac{\partial H_i}{\partial z}\right] \tag{7}$$

Here, $N_i(\xi,\eta)$ $(i = 1,2,3,4)$ is the 2-D isoparametric shape function for the displacement interpolation on the inplane while $H_j(\zeta)$ $(j = 1,2)$ is the 1-D isoparametric shape function for the displacement interpolation along the thickness direction. Thus, the 3-D shape function is obtained from the product of the 2-D and 1-D shape functions, respectively. The composite material property matrices $[D_b]$ and $[D_s]$ are for the bending and transverse shear terms. If the elastic modulus D_z is selected as an arbitrary large number, the third term in Eq. (1) is equivalent to applying the penalty method for the transverse displacements. In order to prevent transverse shear locking, the second term is integrated using a reduced integration technique when low order shape functions are used as in the present element. The nodal displacement vector is expressed as

$$\{d_{local}\}^T = \{\,d_1 \quad d_2 \quad d_3 \quad d_4 \quad d_5 \quad d_6 \quad d_7 \quad d_8\,\} \tag{8}$$

$$\{d_i\} = \{\,u_i \quad v_i \quad w_i\,\} \tag{9}$$

For an analysis of a curved shell structure, the coordinate transformation is conducted from the local coordinate system to the global coordinate system. Let (l_1, m_1, n_1) be the direction cosines between x- and X-axis, (l_2, m_2, n_2) be the direction cosines between y- and Y-axis, and (l_3, m_3, n_3) be the direction cosines between z- and Z-axis. The low case letters indicate the local axes embedded to each shell element while the capital letters denote the global axes. The transformation of displacements between the two coordinate systems result in

$$\begin{Bmatrix} u^i \\ v^i \\ w^i \\ u^{i+4} \\ v^{i+4} \\ w^{i+4} \end{Bmatrix} = \frac{1}{2}\begin{bmatrix} l_1+1 & m_1 & n_1 & l_1-1 & m_1 & n_1 \\ l_2 & m_2+1 & n_2 & l_2 & m_2-1 & n_2 \\ l_3 & m_3 & n_3+1 & l_3 & m_3 & n_3-1 \\ l_1-1 & m_1 & n_1 & l_1+1 & m_1 & n_1 \\ l_2 & m_2-1 & n_2 & l_2 & m_2+1 & n_2 \\ l_3 & m_3 & n_3-1 & l_3 & m_3 & n_3+1 \end{bmatrix}\begin{Bmatrix} U^i \\ V^i \\ W^i \\ U^{i+4} \\ V^{i+4} \\ W^{i+4} \end{Bmatrix} \tag{10}$$

where the superscript 'i' changes from 1 to 4 representing the four nodes at the bottom surface of the plate/shell element. As the transformation matrix in Eq. (10) is denoted by matrix $[T]$ whose size is 24 by 24 for the eight-node shell element, the nodal displacement vector and the element stiffness matrix in terms of the global coordinate system are expressed as

$$\{d_{local}\} = [T]\{d_{global}\} \tag{11}$$

$$[K_{global}] = [T]^T[K_{local}][T] \tag{12}$$

The mass matrix for the shell element is the same as that for the 3-D solid element with the same number of nodes. A diagonal mass matrix may be used to save computational time in conjunction with the explicit time integration scheme. However, for the present analysis, an unconditionally stable implicit time integration scheme such as the Newmark method was selected. The reason is that the time step size for numerical integration is dictated by the CA technique used for the fluid domain as discussed later, and the same time step size is used for both structural and fluid domains. Therefore, it was desired to eliminate any instability associated with structural analysis. The fluid and structural domains were solved in tandem with meeting the interface compatibility conditions such as continuity of velocities and pressure.

2.3. Fluid finite element analysis

The fluid domain was modeled as an acoustic medium. The velocity potential formulation was utilized for the acoustic medium, and it is briefly derived here. The continuity equation is

$$\frac{\partial \rho}{\partial t} + \vec{\nabla}\cdot\rho\vec{u} = 0 \tag{13}$$

where ρ is the density, $\vec{u}$ is the velocity vector, $\vec{\nabla}$ is the gradient operator, and t indicates time. The change of density is expressed as

$$\rho = \rho_o(1+s) \tag{14}$$

in which s is called condensation and ρ_0 is an ambient fluid density. Substitution of Eq. (14) into Eq. (13) with an assumption of $S << 1$ results in

$$\frac{\partial s}{\partial t} + \vec{\nabla}\cdot\vec{u} = 0 \tag{15}$$

The force-balance equation is given as

$$\rho_o\frac{\partial \vec{u}}{\partial t} = -\vec{\nabla}p \tag{16}$$

where p is the pressure. The velocity potential is defined as follows:

$$\vec{u} = -\vec{\nabla}\phi \tag{17}$$

Substitution of the velocity by the velocity potential in Eq. (16) yields

$$\vec{\nabla}\left(-\rho_o\frac{\partial \phi}{\partial t} + p\right) = 0 \tag{18}$$

The relationship $p = Bs$ as well as Eq. (17) are substituted into Eq. (15) as follows:

$$\frac{1}{B}\frac{\partial p}{\partial t} - \nabla^2\phi = 0 \tag{19}$$

where B is the fluid bulk modulus. Elimination of pressure from Eqs. (18) and (19) produces the final wave equation in terms of the velocity potential.

$$\frac{1}{c^2}\ddot{\phi} - \nabla^2\phi = 0 \tag{20}$$

where $c^2 = B/\rho_o$ and c is the speed of sound. Provided with appropriate initial and boundary conditions, this well-posed initial value problem has been much studied and discussed [12].

In order to apply Eq. (20) to FSI problems, the velocity at the FSI interface boundary is computed from the structural dynamics, and it is applied to the wave equation through Eq. (17). On the other hand, the fluid pressure is computed from the wave equation using

$$p = \rho_o\frac{\partial \phi}{\partial t} \tag{21}$$

The acoustic wave equation, Eq. (20), was solved using two different techniques. The first technique used FEM and the second technique utilized CA. Because each technique has pros and cons, both of them were used together to take advantage of each other. For example, the finite element formulation is easy to be coupled at the interface of fluid and structure as well as easy to model complex shape of fluid domain conforming the structural geometry. However, it is computationally expensive and not easy with applying some boundary condition such as the non-reflective boundary condition. On the other hand, the CA technique is computationally very efficient and easy to apply various boundary conditions including the non-reflective boundary condition. However, it is not straightforward to apply the interface compatibility between the fluid and structure as discussed later. Additionally, the CA technique is based on regular lattice geometries like cubes and squares such that it cannot conform a complex shape of fluid domain accurately unless a very dense lattice structure is used. Therefore, the FSI model contains a FEM fluid domain around a FEM structural domain, and the CA fluid domain surrounds the FEM fluid domain. In order to save the computational time, the FEM fluid domain is minimized. Fig. 3 sketches the concept of the overall analysis scheme of the fluid and structural domains.

Applying the Galerkin formulation to the wave equation, the following finite element matrix equation is obtained.

$$\frac{1}{c^2}[M_f]\{\ddot{\phi}\} + [K_f]\{\phi\} = \{F_f\} \tag{22}$$

where

$$[M_f] = \int_\Omega \{H\}^T\{H\}d\Omega \tag{23}$$

$$[K_f] = \int_\Omega \{\nabla H\}^T\{\nabla H\}d\Omega \tag{24}$$

$$\{F_f\} = \int_\Gamma \{H\}^T(\vec{v}\cdot\vec{n})d\Gamma \tag{25}$$

Here, $\{H\}$ is the vector of nodal interpolation functions, Ω and Γ are the fluid domain and boundary, respectively, and $\vec{n}$ is the outward normal vector to the fluid boundary. The right-hand side of Eq. (22) is defined on the boundary of the domain. At the fluid–structure interface, the velocity compatibility provides a convenient input to this finite element problem using Eq. (25).

2.4. Fluid Cellular Automata analysis

Cellular Automata are discrete, rule-based numerical methods that can model complex physical phenomena with relative simplicity. Generally, both space and time are treated discretely and the value of the quantity in question is limited to a finite set of values. As the space–time domain proceeds or grows, the seemingly simple model converges to a complex real-world behavior. The simplicity of the chosen rules and their implementation lowers the computational cost while still achieving required accuracy. The CA rules developed for modeling wave propagation are precursors to the lattice Boltzmann method of modeling fluid flow.

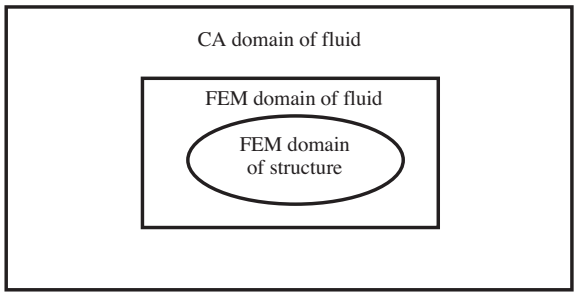

Fig. 3. Sketch showing domains of different analysis techniques.

Following the work in Refs. [8,13–15], the wave equations in 2-D and 3-D use the following rules, respectively:

$$\phi_c(t+\Delta t) = \frac{1}{2}(\phi_w(t) + \phi_E(t) + \phi_S(t) + \phi_N(t) - 2\phi_c(t-\Delta t)) \tag{26}$$

$$\phi_c(t+\Delta t) = \frac{1}{3}(\phi_w(t) + \phi_E(t) + \phi_S(t) + \phi_N(t) + \phi_F(t) + \phi_B(t) - 3\phi_c(t-\Delta t)) \tag{27}$$

The value of ϕ at each interior grid point in the domain of interest (ϕ_c) is updated according to the values at its nearest neighbors. Subscripts 'W', 'E', 'N', 'S', 'F', and 'B' represent west, east, north, south, front and back in terms of the center node denoted by the subscript 'C'. For convenience, the set of points is divided into two sets, "black" and "white" (or "odd" and "even"), such that the neighbors of each white point are all black, and only one "color" is updated during each iteration. The time step size in the CA technique is expressed as

$$\Delta t_{CA} = \frac{\Delta x}{c\sqrt{N_{\dim}}} \tag{28}$$

where Δt_{CA} is the time step size used in the CA technique, Δx is the lattice spacing, c is the speed of sounds in the fluid medium, and $N_{\dim}$ is the lattice dimension which is 2 and 3 for the 2-D and 3-D domains, respectively.

The CA model of the wave equation for velocity potential is simple to implement, and can easily be adapted to a variety of non-trivial boundary conditions. However, converting velocity potential back into useful quantities like pressure and velocity as time- and spatial derivatives is hampered by the alternating update nature of the model. In other words, the CA model has some difficulty to satisfy the compatibility conditions at the fluid–structure interface, like the continuity of velocity and pressure at the interface. Hence, the FEM fluid model was used instead at the fluid–structure interface as sketched in Fig. 3.

Fig. 4 illustrates how to apply common boundary conditions to the CA technique. Boundary conditions are applied using virtual neighbor lattices next to the boundary lattices. When a fixed value boundary condition is applied, there is no need of the virtual lattice. The technique shown in Fig. 4 is applicable for multi-dimensional domain in a straightforward manner.

The two fluid domains, i.e., FEM and CA fluid domains, will overlap such that the outer layer of finite element nodes will be processed as interior CA nodes whose CA-calculated values become FE-specified boundary values. The next set of FEM nodes inside its own domain are calculated by FEM and then passed to the CA domain to serve as neighbors for application of the CA rule to the outer set.

2.5. Numerical modal analysis

Modal analysis extracts the modal parameters like natural frequencies, mode shapes, and damping ratios of a structure. In the experimental modal analysis, multiple sensors are attached to a structure to be tested. Then, an impulse loading is applied to the structure. The sensors mostly used are accelerometers because they are sensitive, small and light so that they may not alter the mass and stiffness of the original structure. On the other hand, velocimeters are bulkier and heavier than accelerometers so that the former sensors are not suitable for a small structure used in a laboratory.

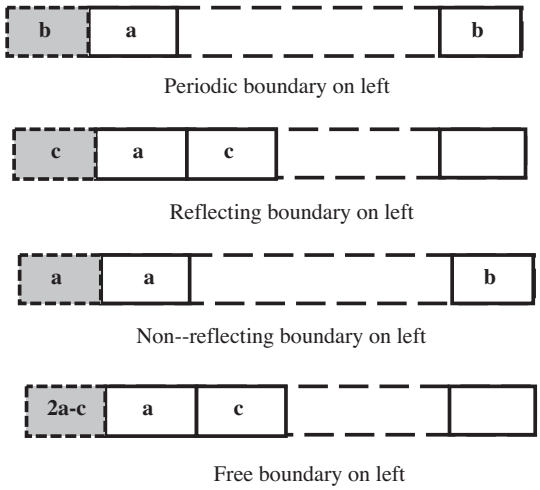

Fig. 4. Application of boundary conditions to CA technique using gray-color virtual lattice values.

In the numerical modal analysis, any dynamic response such as displacement, velocity, acceleration, etc. can be selected. Additionally, much more data can be obtained from the numerical modal analysis because every finite element node provides a time history of the dynamic responses. Once the time domain responses of an excited dynamic structure are obtained, the FFT is used to convert the time domain data into the frequency domain data. Then, the modal parameters are obtained from the frequency domain data at each nodal point. Ref. [16] explained the modal analysis technique to extract the mode shapes. As a result, it is omitted here to save space.

3. Verification study

The computational techniques described in the previous section were tested against some known solutions. The example cases selected for verification were the vibrations of beams in air without FSI. The first example was a cantilever beam. The beam is 1.0 m long, 0.05 m thick, and 0.1 m wide. The modulus of elasticity is 20 GPa and the density is 2000 kg/m^3. The analytical solutions for natural frequencies and mode shapes are available in Ref. [17]. The mode shapes are given in the following equation:

$$\phi(x) = A(\cos\,\beta x - \cosh\beta x) + (\sin\,\beta x - \sinh\beta x) \tag{29}$$

where

$$A = -\frac{\sin\,\beta l + \sinh\beta l}{\cos\,\beta l + \cosh\beta l} \tag{30}$$

$$\beta = \sqrt[4]{\frac{m\omega^2}{EI}} \tag{31}$$

Here, l is the length of the beam, m is the mass per unit length, EI is the beam rigidity, and ω is the frequency in rad/s. The coordinate x is measured from the left end of the beam. The first three mode shapes have $\beta l = 1.875104$ for Mode 1, $\beta l = 4.694091$ for Mode 2, $\beta l = 7.854757$ for Mode 3, from which the natural frequency can be determined.

The numerical modal analysis was conducted to compute the natural frequencies and mode shapes. Additionally, the finite element eigenvalue analysis was also conducted to determine the natural frequencies and mode shapes using the mass and stiffness matrices obtained from the finite element models. Forty beam elements were used for the analysis. Table 1 compares the first three natural frequencies among three different solutions. The values in parenthesis are percentage errors when compared to the analytical frequencies. Figs. 5–7 compare the first three mode shapes of the cantilever beam. The mode shapes obtained from the numerical modal analysis compare very well with the other results from the analytical solution as well as the FEM eigenvalue solution.

The second example was a clamped–clamped beam. The geometric data and material properties are the same as before. The mode shapes can be obtained from Eq. (29) except for the constant A is

$$A = -\frac{\sin\,\beta l - \sinh\beta l}{\cos\,\beta l - \cosh\beta l} \tag{32}$$

The first three mode shapes have $\beta l = 4.730041$ for Mode 1, $\beta l = 7.853205$ for Mode 2, $\beta l = 10.995608$ for Mode 3, from which the natural frequency can be determined. The first three natural frequencies and mode shapes are shown in Table 2 and Figs. 8–10, respectively. The results from the numerical modal analysis agree well with the other solutions.

The previous examples verified the computational procedure for the numerical modal analysis. In the next section, the effect of FSI is considered on the natural frequencies and mode shapes of beams and plates using the multiphysics-based modeling techniques described in the previous section.

4. Study of FSI on composite structures

A composite beam clamped at both ends was studied for the effect of FSI on its dynamic behavior. The geometric and material properties of the beam are the same as those used in the previous section. The water has the density of 1000 kg/m^3, and the speed of sound 1500 m/s. The non-reflected boundary condition was applied to the fluid domain. The numerical modal analysis was conducted using the multiphysics-based computational techniques described in the previous section. As the first study, a short impulse load was applied to the clamped composite beam. Then, the natural frequency and the mode shapes were computed from the numerical modal analysis. In order to obtain the 2nd rotational-symmetric mode shape, the impulse load was applied to a finite element nodal point other than the center. For the center is the node of vibration for the 2nd mode.

The first natural frequency obtained with FSI was 63.64 Hz which is much smaller than the first frequency without FSI as shown in Table 2. The frequency was reduced by more than 60% because of the effect of FSI. This reduction is very comparable to what was measured in the physical experiment for a cantilever beam. The experimental result showed an approximately 70% reduction [9]. Because the cantilever beam is less constrained than the beam clamped at both ends, the effect of FSI was slightly larger. The first two mode shapes are compared in Figs. 11 and 12 between the two cases with and without FSI, respectively. The mode shapes look similar between the two cases. Then, the modal curvatures were compared, which are the second derivatives of the mode shapes and are proportional to the bending strains. As shown in Figs. 13 and 14, there is a much greater difference in the modal

Table 1
Comparison of natural frequencies of cantilever beam in air.

	Analytical solution	FEM eigenvalues analysis	Numerical modal analysis
Mode 1	25.54 Hz	25.54 Hz (0%)	26.20 Hz (2.58%)
Mode 2	160.06 Hz	160.06 Hz (0%)	160.00 Hz (0.03%)
Mode 3	448.19 Hz	448.19 Hz (0%)	460.00 Hz (2.63%)

curvatures than in the mode shapes resulting from the FSI effect, especially for the 2nd mode.

For the next study, the static deflection of the beam clamped at both ends and subjected to a central force was used as the initial condition of the beam, and the beam was freed to vibrate without any external load. Figs. 15 and 16 show snapshots of deformed beams during free vibration of the beam at some selected times. Fig. 15 is for vibration in air while Fig. 16 is for vibration in water. The initial static deflection of the beam is close to its first mode shape. As a result, the first mode shape is the major vibrational mode. The free vibration in air looks like more or less the first mode vibration. However, the free vibration in water shows distinct high frequency modes on top of the first mode. In other words, the FSI resulted in higher mode shapes to store the vibrational energy. This finding was also observed in the previous experiment of a composite cantilever beam [9].

The next set of studies was conducted for a composite plate whose material properties were the same as before. The plate is

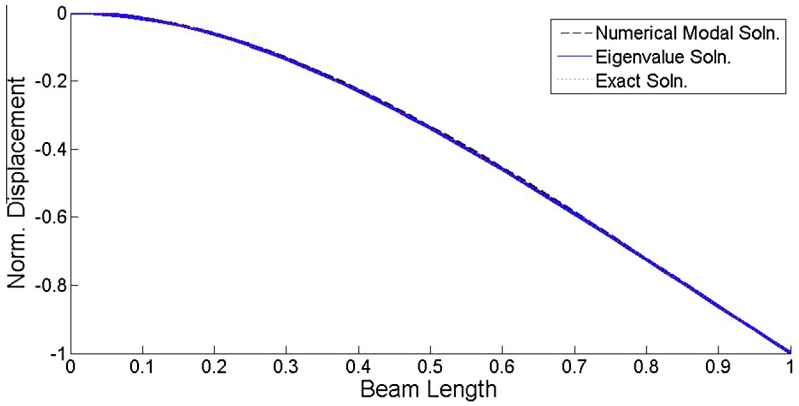

Fig. 5. Comparison of the first mode shape of cantilever beam ends between numerical and analytical solutions.

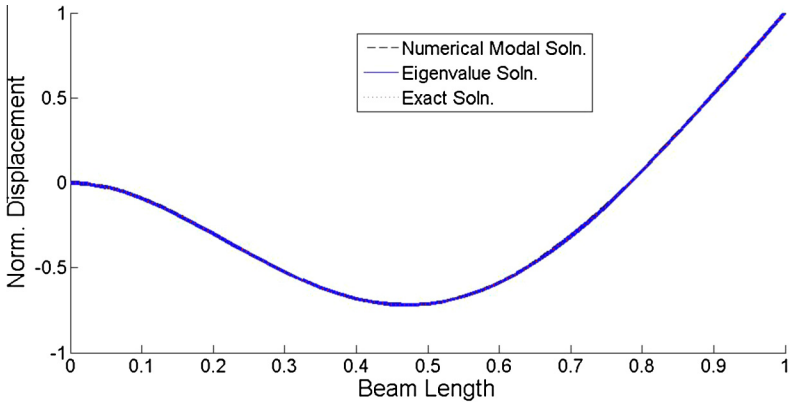

Fig. 6. Comparison of the second mode shape of cantilever beam ends between numerical and analytical solutions.

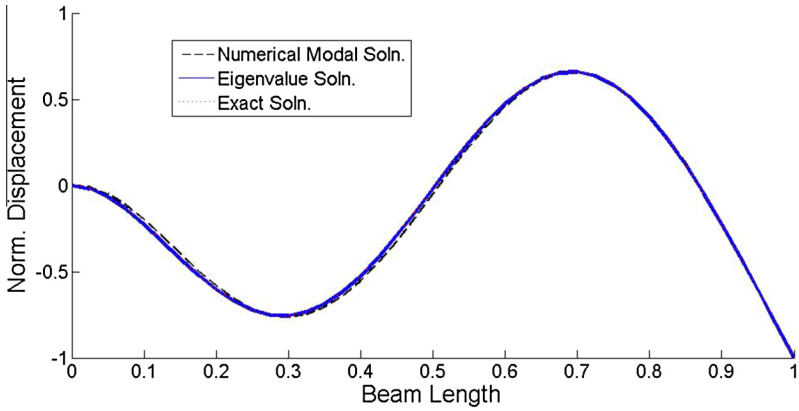

Fig. 7. Comparison of the third mode shape of cantilever beam ends between numerical and analytical solutions.

Table 2
Comparison of natural frequencies of clamped beam at both ends in air.

	Analytical solution	FEM eigenvalues analysis	Numerical modal analysis
Mode 1	162.52 Hz	162.52 Hz (0%)	170.00 (4.6%)
Mode 2	448.01 Hz	448.01 Hz (0%)	460.00 (2.67%)
Mode 3	878.29 Hz	878.29 Hz (0%)	910.00 (3.61%)

square of 1 by 1 m and plate thickness is 0.02 m. A short duration of impulse force was applied to the composite plate while it was clamped all around the boundary. The plate had initially no displacement and velocity. Figs. 17 and 18 plot the deformed shapes of the vibrating composite plate in air and water, respectively, at an arbitrary selected times.

The deformed shape of the vibrating composite plate in air resembles that of the static deformation under the central load as shown in Fig. 17. However, the vibrating composite plate in water shows a different transverse displacement as shown in Fig. 18 where there are local peaks near the four corners of the clamped plate, which were not observed for the vibration in air. Then, the excited mode shapes were compared between the two vibrations in air and water, respectively. Because the force is applied at the center, only symmetric modes were excited by the

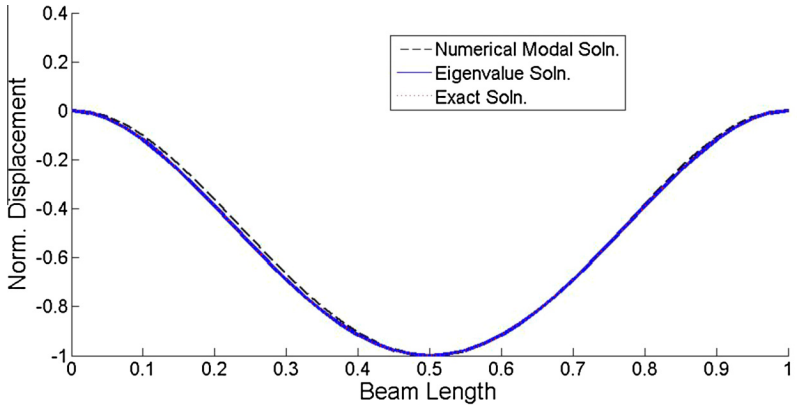

Fig. 8. Comparison of the first mode shape of beam clamped at both ends between numerical and analytical solutions.

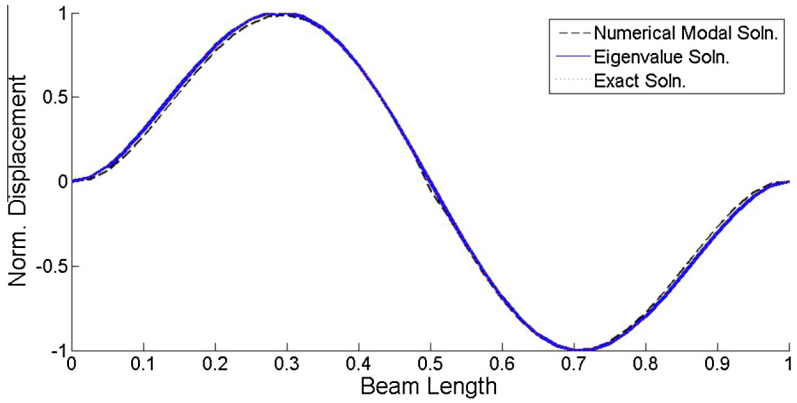

Fig. 9. Comparison of the second mode shape of beam clamped at both ends between numerical and analytical solutions.

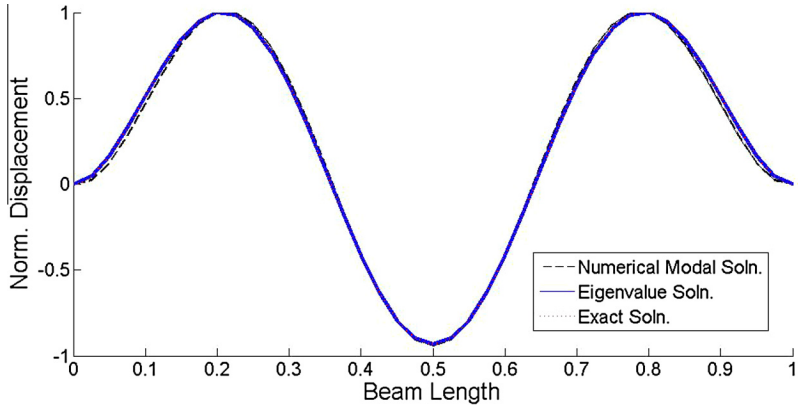

Fig. 10. Comparison of the third mode shape of beam clamped at both ends between numerical and analytical solutions.

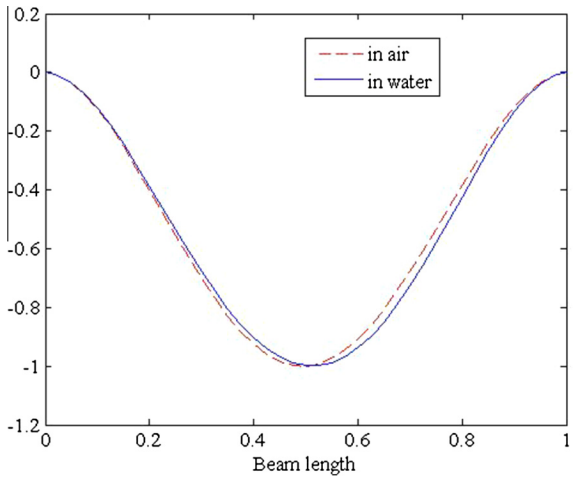

Fig. 11. Comparison of the first mode shape of beam clamped at both ends with and without FSI effect.

impulse load. The first two mode shapes in air are shown in Figs. 19 and 20. The first mode shapes in air and water are very close to each other. However, the next symmetric modes excited by the central impulse force were very different between the vibrations in air and water, respectively. Fig. 20 shows the second symmetric mode excited in air while Fig. 21 shows the counterpart mode in water. The mode shape shown in Fig. 21 explains the local peak deformation near the corners as seen in Fig. 18. This explains the results observed in a previous experiment, where a clamped composite plate was impacted at the center while the plate was in air and water, respectively [6,7]. The study showed that the measured strains were much different near the corners of the plate between the impact in air and under water as shown in Fig. 1(b). That is because the excited mode shapes are different between the vibrations in air and water.

The next examples studied the clamped plate with a given initial condition without any external load. The first study applied the static deformation of the square plate under central force as the initial displacement while the initial velocity was set to zero. The second study applied the static deformation under a concentrated bending moment at the center as the initial displacement. Those initial displacements were obtained from the static bending analysis of the same composite plate clamped along the boundary. The first case corresponds to the initial deformation close to the first

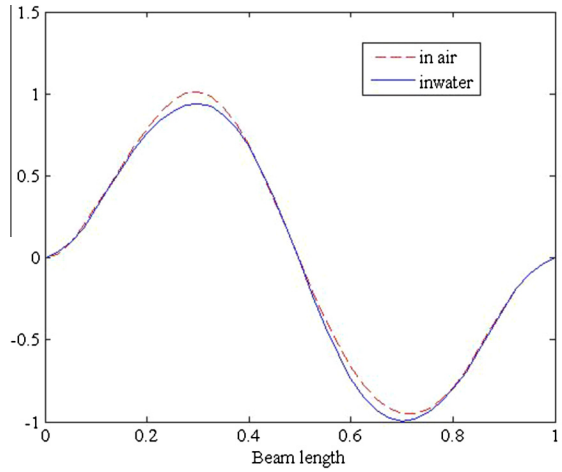

Fig. 12. Comparison of the second mode shape of beam clamped at both ends with and without FSI effect.

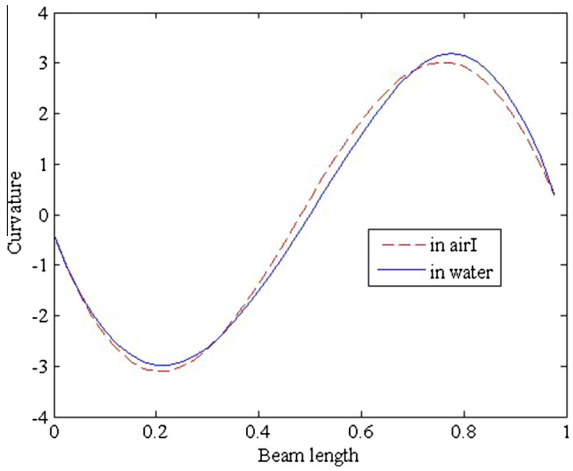

Fig. 13. Comparison of the first modal curvatures o beam clamped at both ends with and without FSI effect.

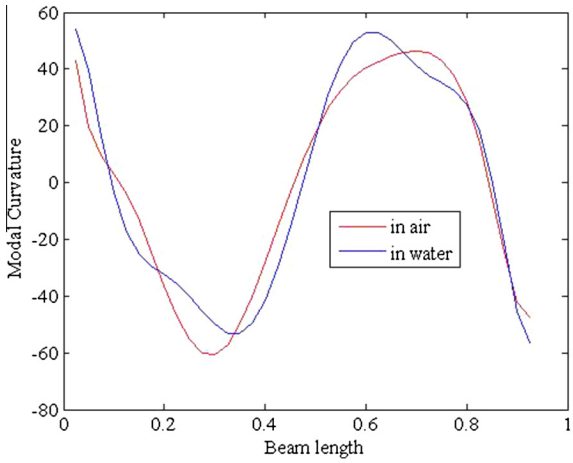

Fig. 14. Comparison of the second modal curvatures of beam clamped at both ends with and without FSI effect.

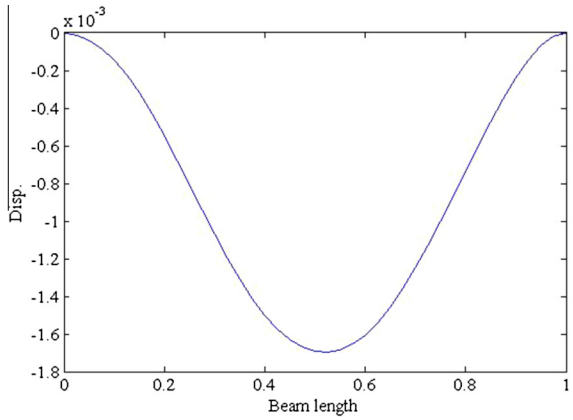

Fig. 15. A snapshot of deformed shape of beam clamped at both end with initial static deflection without FSI.

mode of vibration which is a symmetric mode. On the other hand, the second case corresponds to the initial deformation close to the second mode of vibration which is rotationally symmetric about one axis.

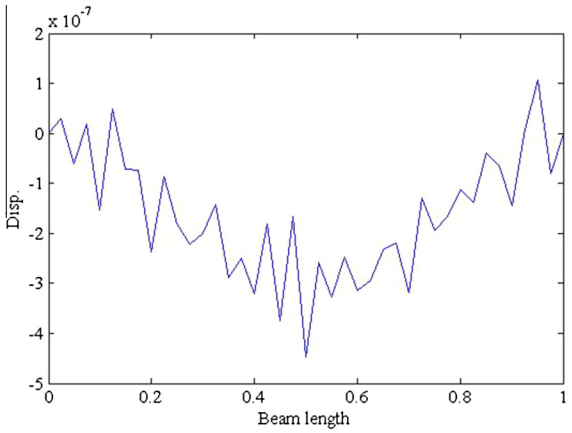

Fig. 16. A snapshot of deformed shape of beam clamped at both end with initial static deflection with FSI.

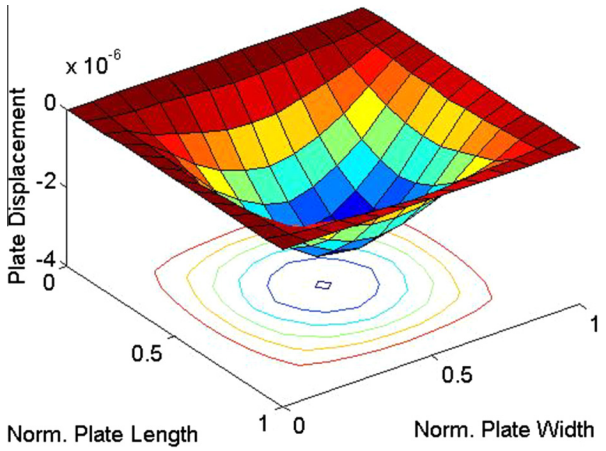

Fig. 17. Vibrational shape of clamped square plate without FSI under impulse load.

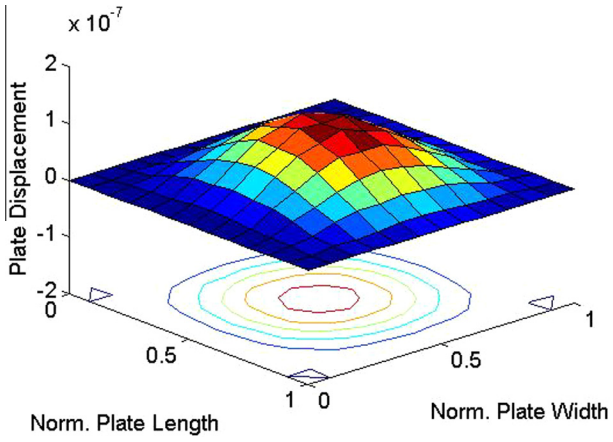

Fig. 18. Vibrational shape of clamped square plate with FSI under impulse load.

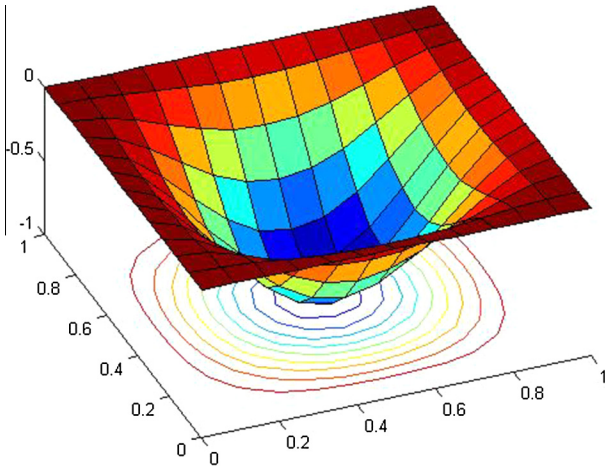

Fig. 19. First mode shape of clamped square plate under central impulse force in air.

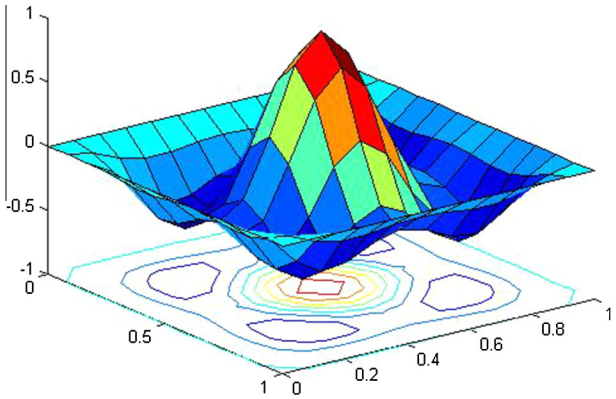

Fig. 20. Second symmetric mode shape of clamped square plate under central impulse force in air.

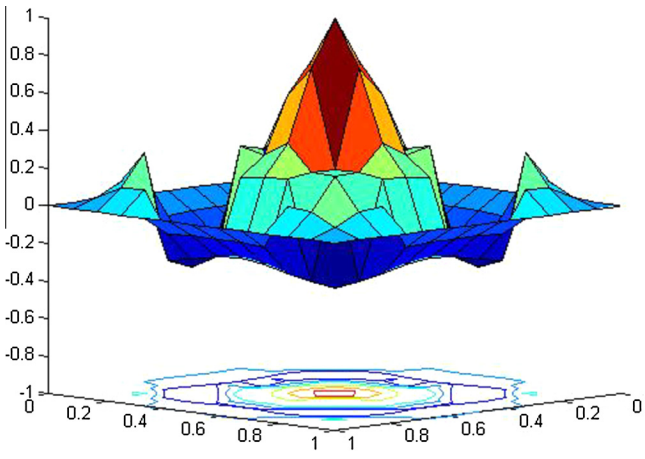

Fig. 21. Second symmetric mode shape of clamped square plate under central impulse force in water.

Snapshots of deformed plates during vibrations in air and water, respectively, at arbitrary times are compared in Figs. 22 and 23 as well as Figs. 24 and 25. The first two figures are for the symmetric initial displacement while the next two figures are for the rotationally symmetric initial displacement. Like the results observed in the beam study, the free vibration of the composite plate in water stored the vibrational energy into modes of higher frequencies as shown in the contour plots, and the transverse deformation during vibration looks much more rugged in water than in air. All deformed plots did not consider slopes for smooth deformed shapes for simplicity. As a result, the deformed plates show facets.

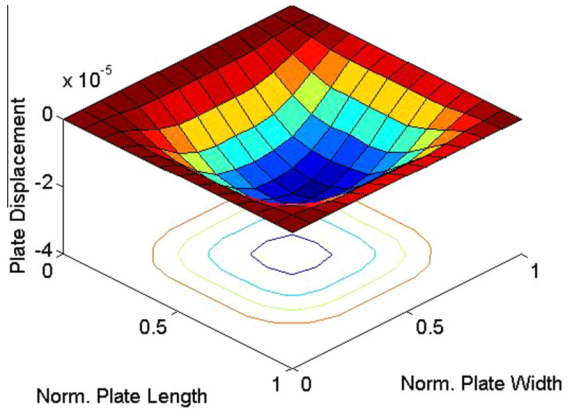

Fig. 22. Snapshot of deformed shape of free vibration of clamped square plate in air with symmetric initial displacement.

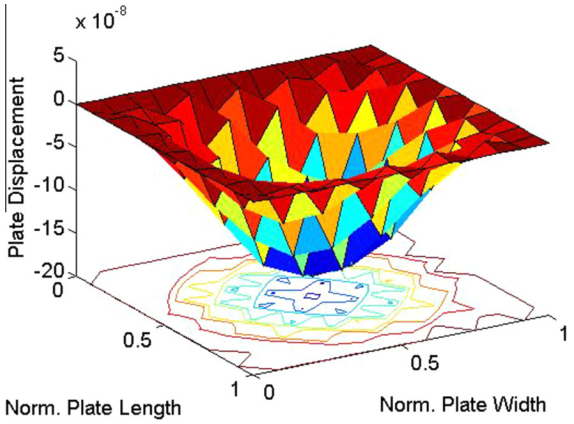

Fig. 23. Snapshot of deformed shape of free vibration of clamped square plate in water with symmetric initial displacement.

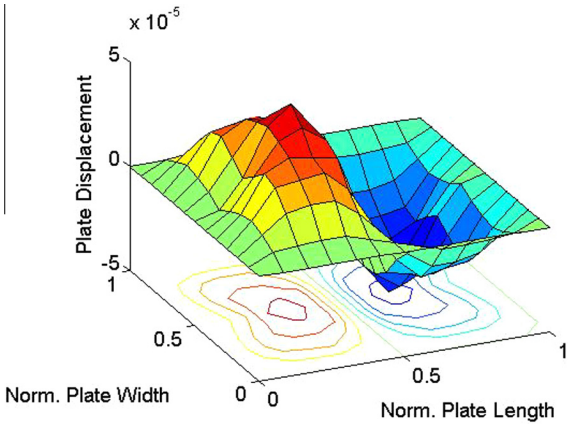

Fig. 24. Snapshot of deformed shape of free vibration of clamped square plate in air with anti-symmetric initial displacement.

The frequency spectra are shown in Figs. 26 and 27 for the symmetric initial displacement, which was obtained from the time history of the central displacement of the plate. The plot for vibration in air shows one sharp peak for the given frequency range, which is the first natural frequency. On the other hand, the frequency spectrum for vibration in water shows the downward shift of the first natural frequency and contributions from various frequency

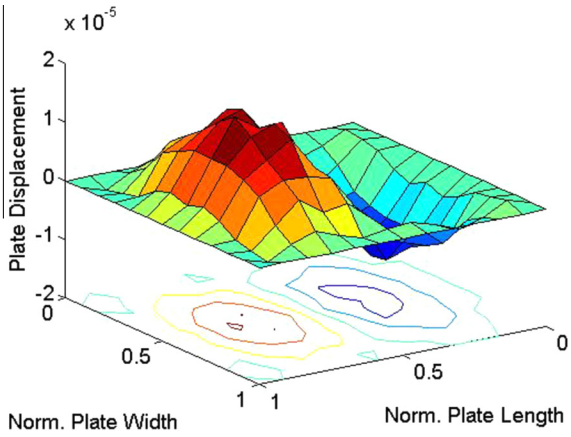

Fig. 25. Snapshot of deformed shape of free vibration of clamped square plate in water with anti-symmetric initial displacement.

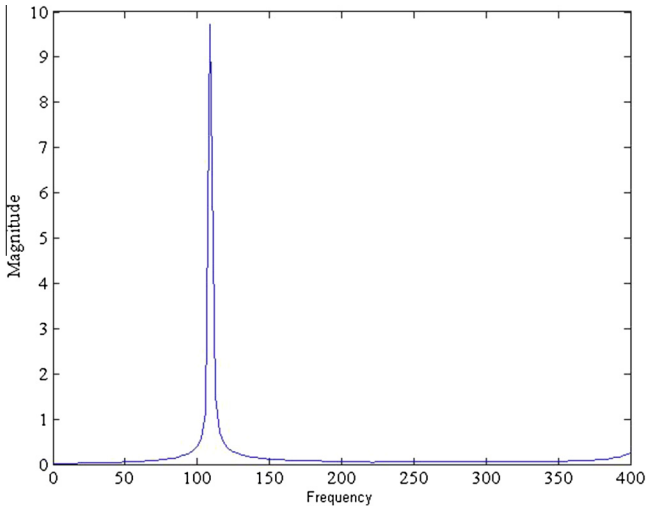

Fig. 26. Frequency spectrum of the center displacement of clamped square plate in air with symmetric initial displacement.

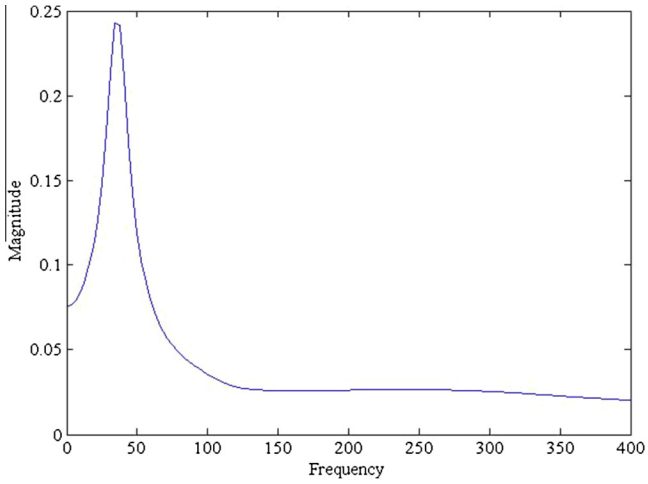

Fig. 27. Frequency spectrum of the center displacement of clamped square plate in water with symmetric initial displacement.

components. Additionally, Figs. 28 and 29 show the frequency spectra of the plate motion with the rotationally symmetric initial displacement. Almost the same kind of observation can be made

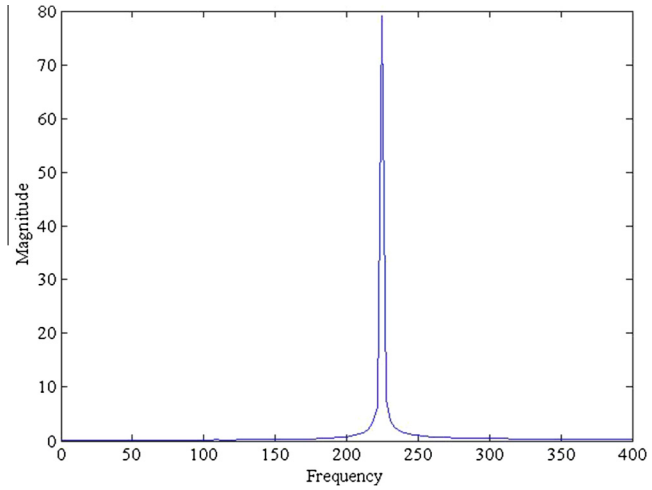

Fig. 28. Frequency spectrum of the center displacement of clamped square plate in air with rotationally symmetric initial displacement.

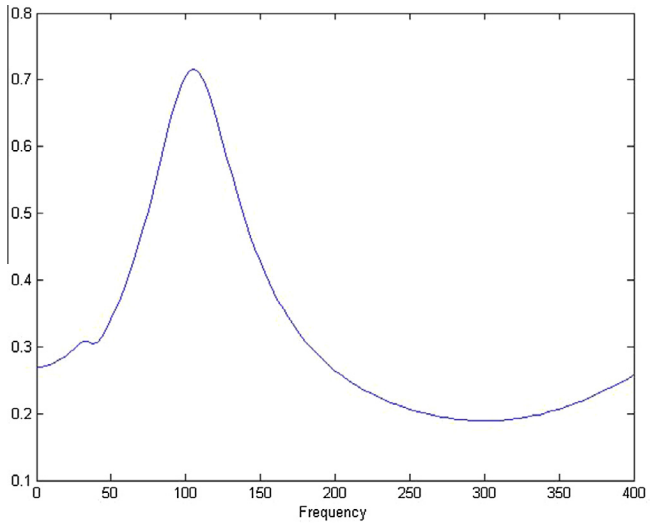

Fig. 29. Frequency spectrum of the center displacement of clamped square plate in water with rotationally symmetric initial displacement.

for the two plots except the frequency in Fig. 28 represents the second mode shape.

5. Conclusions

Numerical modal analyses were conducted to understand the vibrational characteristics such as modal parameters of a polymer composite beam and plate when they were submerged in water. The composite structures were modeled using FEM with displacement degrees of freedom only elements. The water domain was divided into two subdomains. The FEM was applied to the inside small fluid subdomain containing the structure while the CA technique was used for the much larger fluid subdomain surrounding the former fluid subdomain. By doing so, the FSI could be undertaken easily with saving in the computational cost associated with the fluid analysis which was assumed to be an acoustic medium with negligence of fluid flow and viscosity.

The modal parameters such as natural frequencies, mode shapes, modal curvatures were compared between the two cases; a structure in air and water, respectively. The comparison showed that not only the natural frequencies but also mode shapes and modal curvatures were influenced by FSI. This finding was a confirmation of the results obtained previously for composite beams using the experimental modal analysis [9]. Additionally, the analysis of a clamped composite plate showed that the second symmetric mode shape in water was very different from that in air, and the mode shape explained what was observed with an impact test of a composite plate in water, i.e., such a drastic difference in the strain responses near the corner of the plate between the two cases; impacted plate in water and air, respectively as compared in Fig. 1.

Free vibrational analysis of the composite beam and plate released from an initial static deflection showed that the FSI effect activated high frequency modal components of the composite structures. The frequency spectrum showed a major difference between the two cases, with and without FSI effect. All the differences as explained above affected the dynamic responses of polymer composite structures in water, which could result in premature failure as well as a shift in the failure location because of the FSI effect when compared to those without FSI.

Acknowledgment

This work was supported by the Office of Naval Research (ONR) Solid Mechanics Program. The program manager is Dr. Yapa D.S. Rajapakse.

References

[1] Pal N, Bhattacharyya S, Sinha P. Coupled slosh dynamics of liquid-filled, composite cylindrical tanks. J Eng Mech 1999;125(4):491–5.
[2] Pal NC, Bhattacharyya SK, Sinha PK. Non-linear coupled slosh dynamics of liquid-filled laminated composite containers: a two dimensional finite element approach. J Sound Vib 2003;261(4):729–49.
[3] Gong SW, Lam KY. Transient response of floating composite ship section subjected to underwater shock. Compos Struct 1999;46(1):65–71.
[4] LeBlanc J, Shukla A. Dynamic response and damage evolution in composite materials subjected to underwater explosive loading: an experimental and computational study. Compos Struct 2010;92(10):2421–30.
[5] Kwon YW. Study of fluid effects on dynamics of composite structures. ASME J Pressure Vessel Technol 2011;133:031301–31306.
[6] Kwon YW, Violette MA, McCrillis RD, Didoszak JM. Transient dynamic response and failure of sandwich composite structures under impact loading with fluid structure interaction. Appl Compos Mater 2012;19(6):921–40.
[7] Kwon YW, Conner RP. Low velocity impact on polymer composite plate in contact with water. Int J Multiphys 2012;6(3):179–97.
[8] Craugh LE, Kwon YW. Coupled finite element and cellular automata methods for analysis of composite structures with fluid–structure interaction. Compos Struct 2013;102:124–37.
[9] Kwon YW, Priest EM, Gordis JH. Investigation of vibrational characteristics of composite beams with fluid–structure interaction. Compos Struct 2013;105:269–78.
[10] Kwon YW. Dynamic responses of composite structures in contact with water while subjected to harmonic loads. Appl Compos Mater 2014;21:227–45.
[11] Kwon YW. Analysis of laminated and sandwich composite structures using solid-like shell elements. Appl Compos Mater 2013;20(4):355–73.
[12] Farlow SJ. Partial differential equations for scientists and engineers. New York: Dover Publications Inc.; 1993.
[13] Chopard B, Droz M. Cellular automata modeling of physical systems. Cambridge: Cambridge University Press; 1998.
[14] Chopard B. A cellular automata model of large-scale moving objects. J Phys A: Math General 1990;23(10):1671–87.
[15] Kwon YW, Hosoglu S. Application of lattice Boltzmann method, finite element method, and cellular automata and their coupling to wave propagation problems. Comput Struct 2008;86(7–8):663–70.
[16] Inman DJ. Engineering vibration. Englewood Cliffs, NJ: Prentice Hall; 1994.
[17] Tse FS, Morse IE, Hinkle RT. Mechanical vibrations, theory and applications. 2nd ed. Boston, MA: Allyn and Bacon, Inv.; 1978.